



Formation of Quiescent Prominence Magnetic Fields by Supergranulations

Qingjun Liu¹ and Chun Xia^{1,2} ¹ School of Physics and Astronomy, Yunnan University, Kunming 650500, People's Republic of China; chun.xia@ynu.edu.cn² National Astronomical Observatories, Chinese Academy of Sciences, Beijing 100101, People's Republic of China

Received 2022 June 10; revised 2022 July 8; accepted 2022 July 8; published 2022 July 22

Abstract

To understand the formation of quiescent solar prominences, the origin of their magnetic field structures, i.e., magnetic flux ropes (MFRs), must be revealed. We use three-dimensional magnetofriction simulations in a spherical subdomain to investigate the role of typical supergranular motions in the long-term formation of a prominence magnetic field. Time-dependent horizontal supergranular motions with and without the effect of Coriolis force are simulated on the solar surface via Voronoi tessellation. The vortical motions by the Coriolis effect at boundaries of supergranules inject magnetic helicity into the corona. The helicity is transferred and accumulated along the polarity inversion line (PIL) as a strongly sheared magnetic field via helicity condensation. The diverging motions of supergranules converge opposite magnetic polarities at the PIL and drive the magnetic reconnection between footpoints of the sheared magnetic arcades to form an MFR. The magnetic network, negative-helicity MFR in the northern hemisphere, and fragmented-to-continuous formation process of magnetic dip regions are in agreement with observations. Although diverging supergranulations, differential rotation, and meridional flows are included, the simulation without the Coriolis effect cannot produce an MFR or sheared arcades to host a prominence. Therefore, Coriolis force is a key factor for helicity injection and the formation of magnetic structures of quiescent solar prominences.

Unified Astronomy Thesaurus concepts: Solar prominences (1519); Supergranulation (1662); Solar magnetic fields (1503); Magnetohydrodynamical simulations (1966)

Supporting material: animations

1. Introduction

Quiescent prominences and filaments are long thin structures of dense and cool plasma that remain stable in the solar corona for days or weeks along the polarity inversion lines (PILs) of quiescent regions (Parenti 2014). Their magnetic fields have special structures, the so-called filament channels, which support the dense mass against gravity (Mackay et al. 2010). The aligned chromospheric fibrils at two sides of a filament (Foukal 1971) and dominant magnetic field components along the PILs of prominences (Leroy et al. 1983) indicate that filament channels have strongly sheared magnetic fields. The overall magnetic topology of quiescent filament channels is most likely a helical magnetic flux rope (MFR) (Xia et al. 2014b, 2014a; Xia & Keppens 2016), with plenty of observational evidence, such as the elliptical shape of coronal cavities around quiescent prominences (Gibson et al. 2010), concentric rings of Doppler velocity in coronal cavities (Bak-Stęślicka et al. 2013), persistent swirling motions of coronal plasma around the center of coronal cavities above prominences (Wang & Stenborg 2010), and the inverse polarity of a prominence magnetic field whose component perpendicular to the PIL is opposite to the one of a potential field (Bommier et al. 1994). Dipped sheared arcades with concave-up magnetic fields (DeVore & Antiochos 2000) may be the magnetic structure of short filament channels around active regions, but not long ones in quiescent regions (Patsourakos et al. 2020).

Two mechanisms were proposed to explain the formation of MFRs in the corona. The first mechanism suggests that the emergence of the upper part of an MFR from the conversion zone into the corona leads to sheared magnetic arcades (SMAs), arcade-like magnetic loops without concave-up magnetic fields, which are then transformed into an MFR through magnetic reconnection (Fan 2001). However, this flux emergence mechanism does not apply to the filaments in quiescent regions where no large-scale magnetic flux emergence was found (Mackay et al. 2008). Statistical study of filament observations reveals that over 90% of filaments lie above PILs external to conjugate bipolar fields by flux emergence (Mackay et al. 2008). The second mechanism relies on the shearing, converging, and cancellation of opposite-polarity magnetic flux on the photosphere, which transforms SMAs into a helical MFR by magnetic reconnection in the lower solar atmosphere (Van Ballegooijen & Martens 1989). This flux cancellation mechanism has been supported by many numerical simulations from magnetofriction models (Mackay & Van Ballegooijen 2006) and zero-beta magnetohydrodynamic (MHD) models (Amari et al. 1999) to isothermal MHD models (Xia et al. 2014b). However, these models were confronted with three difficulties. First, these models use smooth magnetic flux distributions, which contradict the observational fact that the photospheric magnetic flux under quiescent filaments is discrete and concentrated as small elements at supergranular boundaries (Zhou et al. 2021). Second, the models relied on large-scale systematic converging flows or equivalent magnetic flux diffusion toward the PIL on the photosphere to drive the flux cancellation. But observations have not found such large-scale flows; instead, supergranular-scale converging flows between diverging supergranules were found both inside and outside filament channels (Rondi et al. 2007; Schmieder et al. 2014). Third, the models required large-scale



Original content from this work may be used under the terms of the [Creative Commons Attribution 4.0 licence](https://creativecommons.org/licenses/by/4.0/). Any further distribution of this work must maintain attribution to the author(s) and the title of the work, journal citation and DOI.

shearing motions, such as differential rotation, to get shear arcades. However, the differential rotation injects helicity of the opposite sign into west–east-oriented PILs, in contrast to the observed hemispheric preference (van Ballegoijen et al. 1998), which manifests in filaments with negative (positive) helicity dominating in the northern (southern) hemisphere (Ouyang et al. 2017).

Antiochos (2013) proposed the helicity condensation theory to explain the formation of filament channels. In the theory, photospheric vortical motions between the convective cells inject magnetic helicity into magnetic flux tubes, and coronal magnetic reconnections between neighboring flux tubes transfer the injected twist toward the outer periphery of the flux tubes, leading to an inverse cascade of magnetic helicity from small scales to the largest scale at the periphery of the whole magnetic flux system along the PIL, where the helicity condenses and SMAs appear. The theory was demonstrated by ideal MHD simulations based on topological coronal models between two parallel plates (Knizhnik et al. 2015; Zhao et al. 2015) and a Cartesian coronal model with a circular PIL (Knizhnik et al. 2017). These numerical models ignored the primary diverging flows of supergranular cells and simplified the observed cyclonic vortices between the anticyclonic flows of supergranules (Duvall & Gizon 2000; Langfellner et al. 2015) caused by the Coriolis force (Hathaway 1982; Egorov et al. 2004), as many annular vortical flows inject magnetic helicity into the corona and produce the SMAs along PILs. Using a large-scale averaged representation of the small-scale vortical motions in magnetofriction simulations, Mackay et al. (2014) found that the helicity condensation can overcome the incorrect sign of helicity injection from differential rotation on a west–east-oriented PIL and help form MFRs in filament channels. In this Letter, we investigate the role of supergranular flows in the formation of the magnetic field of quiescent prominences via magnetofriction simulations.

2. Numerical Methods

The simulation domain is a spherical subdomain extending over radii $r \in [1R_\odot, 1.5R_\odot]$, colatitudes $\theta \in [39^\circ.6, 90^\circ]$, and longitudes $\phi \in [0^\circ, 60^\circ]$ with a four-level adaptive mesh refinement (AMR) to get 256^3 effective resolution. From a smooth bipolar photospheric magnetogram, we use the spherical potential field extrapolation module in the PDFI_SS software (Fisher et al. 2020) to extrapolate the initial potential magnetic field. We solve the magnetofriction equations (Guo et al. 2016) without explicit resistivity using the code MPI-AMRVAC (Porth et al. 2014; Xia et al. 2018). Magnetic reconnection here is caused by numerical resistivity. The magnetofrictional velocity $\mathbf{v} = \mathbf{J} \times \mathbf{B}/(\nu_0 B^2)$, where $\nu_0 = 10^{-15}$ s cm $^{-2}$ is the viscous coefficient, has a smooth decay to zero toward the photosphere (Cheung & DeRosa 2012), and an upper limit of 30 km s $^{-1}$ (Pomoell et al. 2019). We use the constrained transport (CT) scheme (Gardiner & Stone 2005), with the HLL flux for the electric field, on the staggered AMR mesh (Olivares et al. 2019) to keep the magnetic field divergence free. Boundary conditions are periodic on the longitudinal boundaries, open on the outer radial boundary, and closed on the latitudinal boundaries. On the photospheric boundary, we use zero normal velocity with the supergranular horizontal velocity field described as follows.

A Voronoi tessellation of the solar surface resembles (super)granular segmentation in both topology and statistics

(Schrijver et al. 1997). We use a weight function $\omega = 3|\sin(\pi t/\tau + \xi)| + 0.7$ to generate Voronoi tessellation, in which τ is the lifetime of a supergranular cell with a Gaussian random distribution centered on 1.6 days (Hirzberger et al. 2008) and ξ is the random initial phase. We use 1 as the lower limit of the weights for living cells; smaller weights are set to zero to remove the corresponding cells from the tessellation map. So, the simulated supergranular cells are changing with time with their area proportional to their weights. We adopt the dimensionless diverging velocity within supergranular cells as $v_r(r) = 2r^2/r_0 \exp(-4r^2/r_0^2)$ (Gudiksen & Nordlund 2005), where r is the spherical distance to the cell center and r_0 is the radius of a circle with area equal to the supergranular cell. The vortical velocity due to Coriolis force acting on the diverging horizontal flows is simplified as $v_\theta(r) = 2r/r_0 v_r(r)$, ignoring the latitude dependence of the Coriolis force. We use a normalization factor to make sure the maximal supergranular speed is initially 500 m s $^{-1}$. The velocities of differential rotation and meridional flow (Mackay et al. 2014) are also included. We multiply the total driving speed by 5 to speed up the long-term evolution. Dimensionless values in our results have the time unit of 8.3 hr and the magnetic field unit of 2 G. We ran the model SR with supergranules rotating under Coriolis force and the model SS without the Coriolis effect.

3. Results

Initially (Figure 1(a)), the magnetic field is a bipolar arcade rooted in the smooth positive (red) and negative (blue) polarity regions separated by a straight north–south-directed PIL. Then, the supergranular diverging flows transport and concentrate magnetic flux to the boundaries of supergranules, forming a magnetic network, and the differential rotation gradually shifts the northern part of the magnetic flux to the east and the southern part to the west, making the PIL tilted counter-clockwise. At time 30 (Figure 1(b)), short magnetic loops near the PIL have skewed away from the initial potential field state. The skew angle, defined as the angle between the horizontal component of the magnetic field above the PIL and the horizontal direction perpendicular to the PIL (Mackay & van Ballegoijen 2001), is about 45° . Long loops, which root in the central region of each polarity far from the PIL, remain in an approximately potential state with negligible skew angles during the whole evolution. At time 60 (Figure 1(c)), low-lying magnetic loops near the PIL are almost aligned with the PIL with large skew angles, and some of them are changed into helical field lines (red line) along the PIL. At time 90 (Figure 1(d)), more helical field lines form and enwind the earlier-born helical lines, assembling a low-lying, thin MFR along the PIL. Later, at time 120 (Figure 1(e)), which is after 41.5 days, the MFR matures with a larger height and cross-section size suitable for hosting a quiescent prominence. Different from earlier MFR models in which helical field lines root in two compact regions, the footpoints of this MFR are distributed extensively along the PIL. In contrast to model SR, model SS does not produce any MFR or SMAs until time 120 (Figure 1(f)), and all magnetic loops stay nearly potential for another 120 time units.

To understand the origin of the sheared magnetic loops, we illustrate the buildup process of the sheared loops of model SR in the left column of Figure 2. For comparison, a similar representation of model SS at the same time is plotted in the

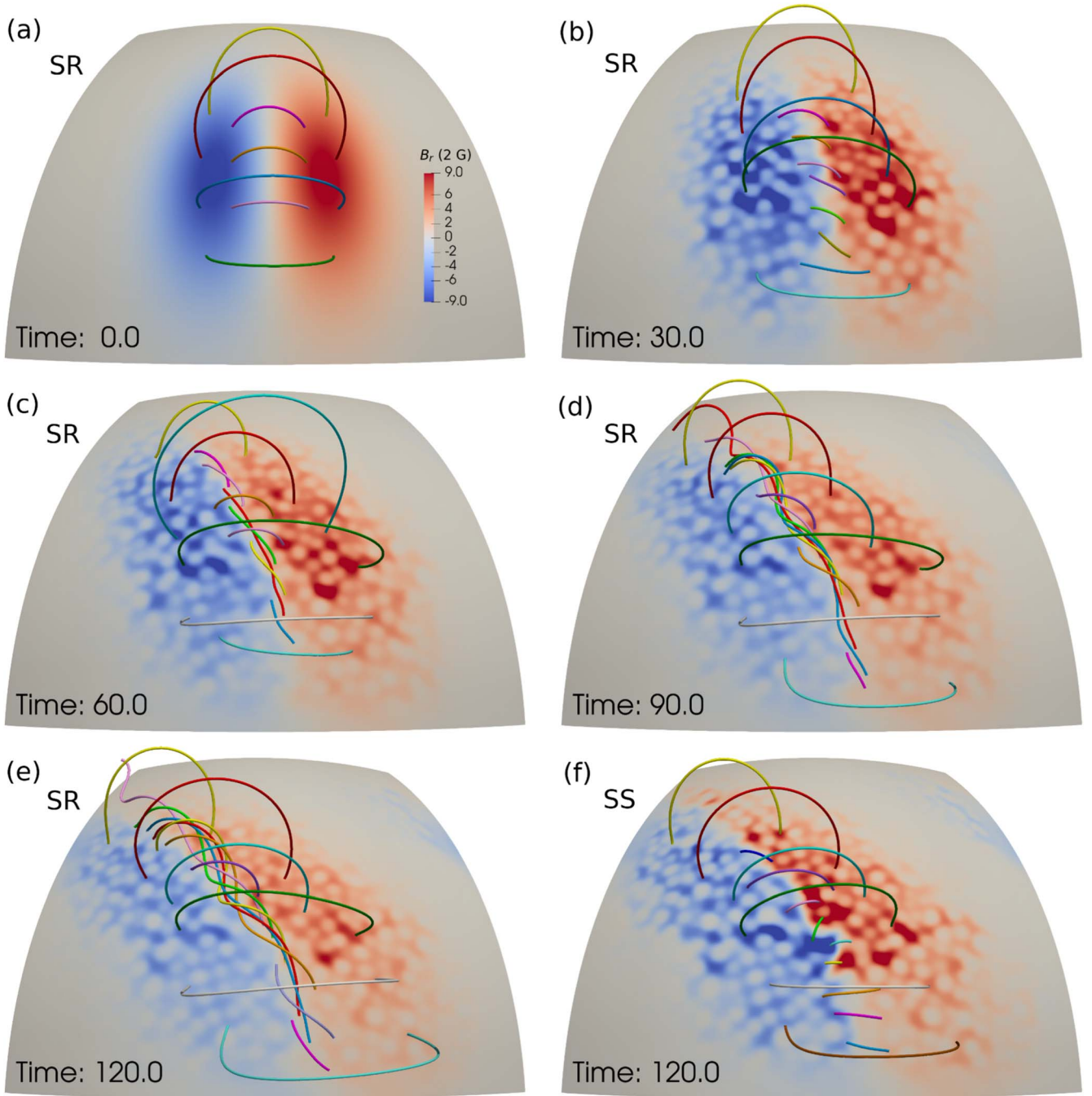


Figure 1. Magnetic field lines of model SR with the Coriolis effect at time 0 (a), 30 (b), 60 (c), 90 (d), and 120 (e) in contrast to model SS without the Coriolis effect at time 120 (f). The photosphere is colored by the radial magnetic field in red-to-blue colors saturated at ± 18 G. An animation of the evolution of the magnetic field lines in model SR is available. The animation proceeds from time 0 to 120 in steps of 0.6.

(An animation of this figure is available.)

right column. In panels (a)–(f), the magnetic loops crossing over the cyan PIL at different heights are plotted in rainbow colors. At time 15, the lowest blue loop in model SR has a short length and a small skew angle to the PIL, while the loops in model SS have nearly zero skew angles. For model SR at later times 45 and 60, several loops close to the PIL are sheared and the lowest loop has the fastest growth rate in skew angle and length. Farther away from the PIL, loops with higher altitudes have smaller skew angles. In contrast, loops in model SS at all heights and distances from the PIL remain roughly perpendicular to the PIL. The sheared loops with large skew angles in

model SR are not created by persistent photospheric shearing flows, because such shearing flows along the PIL do not exist. Instead, only vortical diverging and converging flows by supergranules exist as shown by gray arrows in panels (g) and (h). A logical explanation for the strongly sheared loops around the PIL in model SR is referable to helicity condensation theory (Antiochos 2013). Vortical converging flows toward the junctions of several supergranules inject negative magnetic helicity into the magnetic flux tubes with footpoints in strong magnetic flux on the photosphere. Component magnetic reconnection happens on the interface of adjacent twisted flux

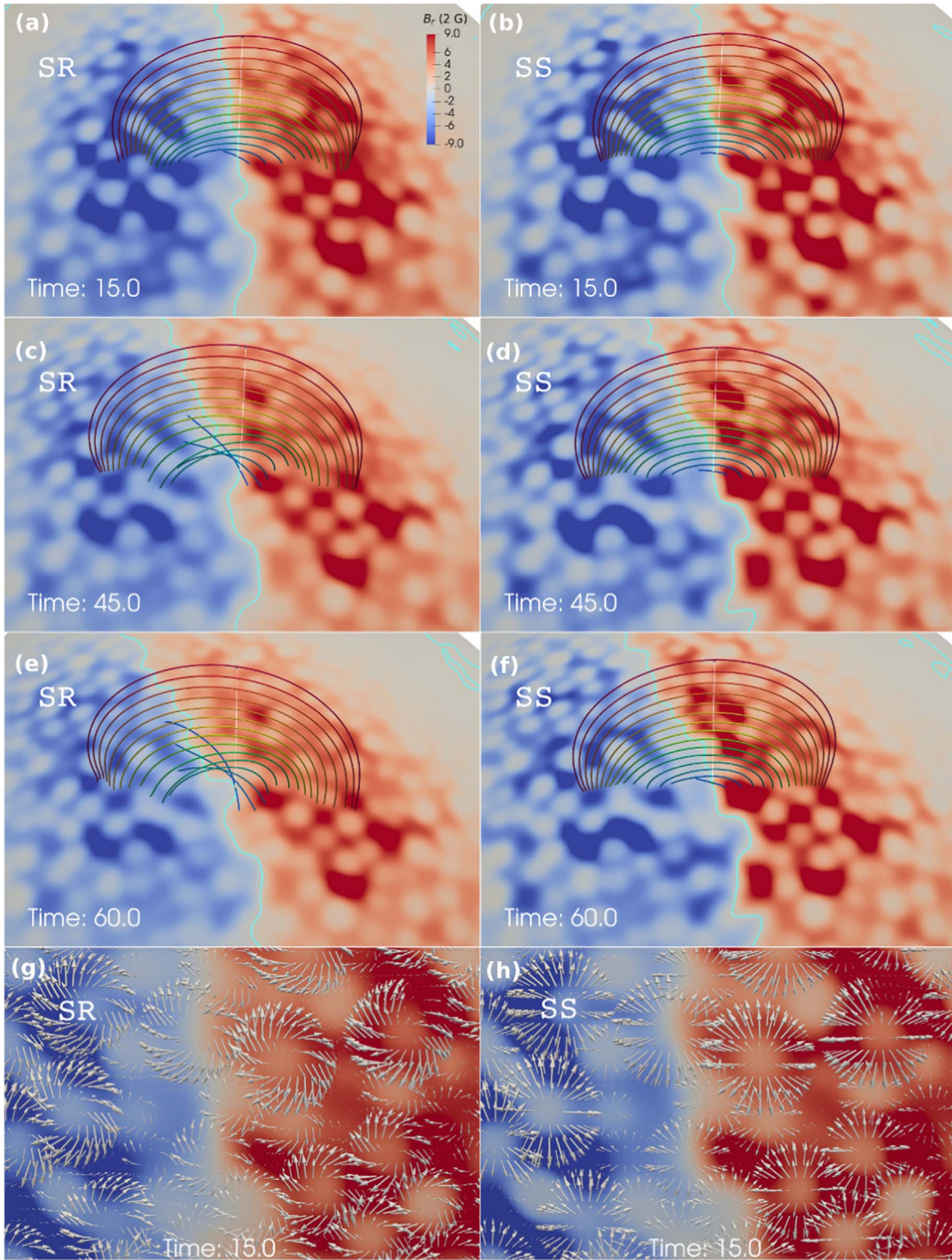


Figure 2. Comparative views of model SR and SS at times 15, 45, and 60. In panels (a)–(f), magnetic field lines, in rainbow colors, are integrated from uniformly sampled seed points along a radial white line starting from the cyan PIL at a fixed latitude. The photosphere is colored by a radial magnetic field saturated at ± 20 G. Zoom-in views at time 15 are shown in panels (g) and (h), where gray arrows present the photospheric horizontal velocity field.

tubes, which transports the twisted flux to the common periphery of the flux tubes and leaves behind the untwisted flux in the central regions. This process inversely cascades from small scales to large scales until it reaches the biggest flux tube representing the whole bipolar region with part of the

periphery folded around the PIL, where twisted fluxes with negative helicity condense as SMAs.

Then we present how much the magnetic helicity is injected into the corona and how the magnetic free energy is stored in our models. The flux of (relative) magnetic helicity through the photosphere is defined by the equation with zero resistivity

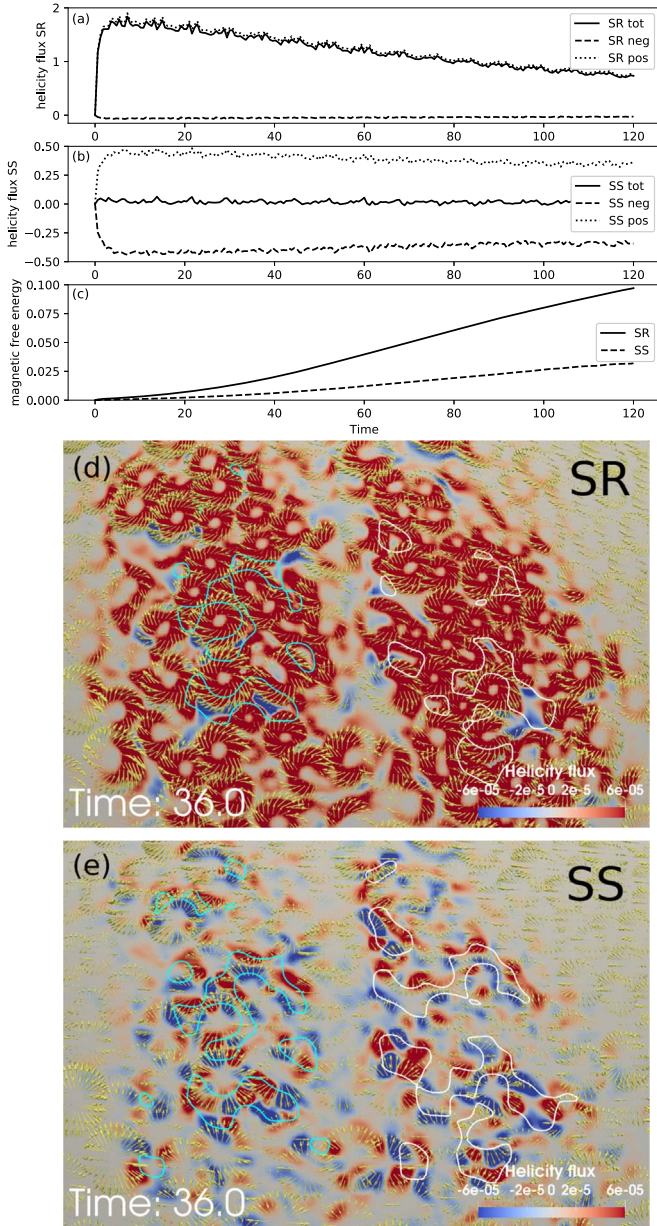


Figure 3. (a) Time evolution of the magnetic helicity fluxes as the total (solid line), the negative (dashed line), and the positive (dotted line) ones through the photosphere of model SR. (b) Similar curves as (a) for model SS. (c) Time evolution of the magnetic free energy of models SR (solid line) and SS (dashed line). (d) Magnetic helicity flux density on the photosphere overlaid with a horizontal velocity field as yellow arrows and contours of B_r at ± 16 G for model SR at time 36. (e) Similar plot to (d) for model SS.

(Berger & Field 1984):

$$\frac{dH_R}{dt} = -2 \int A^P \times E \cdot dS = -2 \int (A_\theta^P E_\phi - A_\phi^P E_\theta) dS, \quad (1)$$

where A^P is the vector potential of the potential magnetic field, which matches the instantaneous photospheric B_r , E is the electric field and quantified as the electric field from the CT scheme, and dS is the surface element with normal direction \hat{r} . Figure 3(a) shows the time evolution of the magnetic helicity fluxes through the photosphere in model SR as the total (solid line), the negative (dashed line), and the positive flux (dotted line). The positive helicity flux is about 20–30 times larger than

the negative-helicity flux. Magnetic helicity fluxes through other boundaries are negligible. The photospheric distribution of the integrand in Equation (1) is shown in Figure 3(d) with horizontal velocity vectors and contours of B_r overplotted. The positive values of the integrand are distributed in the outer regions of supergranules in donut shapes, induced by the clockwise-rotating diverging flows of supergranules. The negative values are distributed sporadically along the borders of several supergranules and caused by irregular counter-clockwise converging flows toward strong magnetic flux. For model SS as shown in panel (b), the positive- and negative-helicity fluxes almost cancel out with a small positive total flux. Panel (e) for model SS shows that positive values alternate with negative values in the outer region of supergranules. Figure 3(c) presents the time evolution of the magnetic free energy, which is obtained by subtracting the potential field energy from the total magnetic energy. Both models have increasing magnetic free energy, while the magnetic free energy increases about three times faster in model SR than in model SS.

Long-lived prominence plasma should be supported by magnetic tension force against downward gravity in locally concave-up magnetic fields, i.e., magnetic dips. We locate the magnetic dip regions (MDRs) where the radial component of the curvature of magnetic field lines is positive and the radial component of the magnetic field has less than 10% proportion. Figure 4 presents snapshots of the formation of magnetic dips from the top views in upper panels (a)–(b) and from the side views in lower panels (a1)–(b1). At time 61.2, small isolated MDRs are distributed along the PIL with supergranular-scale intervals. Later, at time 82.8, the small MDRs grow horizontally along the PIL and connect to form three long MDRs. Helical field lines tangential to the photosphere outline the periphery of an MFR above the PIL and the MDRs naturally appear in the lower half of the MFR. At time 120, further growth and connection of MDRs result in a long slab-like MDR with a growing height reaching 28,000 km and a length of about 480,000 km. The MFR surrounding the MDR has helical field lines winding one to two turns around a common axis. If the MDRs are filled with prominence plasma, the formation process of MDRs is consistent with filament observations showing that quiescent filaments form from aligned fragments to a continuous body (Pevtsov & Neidig 2005).

To understand the transition from SMAs to MFRs, we find the sites of magnetic reconnection and flux cancellation on the photosphere. In Figure 5(a), the footpoints of the pink and the sky-blue field line, in the middle of the panel, converge to the white PIL by adjacent supergranular flows indicated by the purple arrows, and the two field lines are about to be reconnected at the PIL to form a helical field line like the yellow one. Similarly, the blue and the red field line will reconnect to form a helical field line like the green one in the lower-right region. Figure 5(b) presents a zoom-out side view of these field lines above the photospheric supergranular cells. The sites of magnetic reconnection are at the borders of supergranular cells on two sides of the PIL. Some parts of the PIL crossing through supergranular cells are bald patches where the MFR touches the photosphere. Evidence of magnetic flux cancellation is shown in Figure 5(c) in which the time evolution of the total unsigned magnetic flux on the

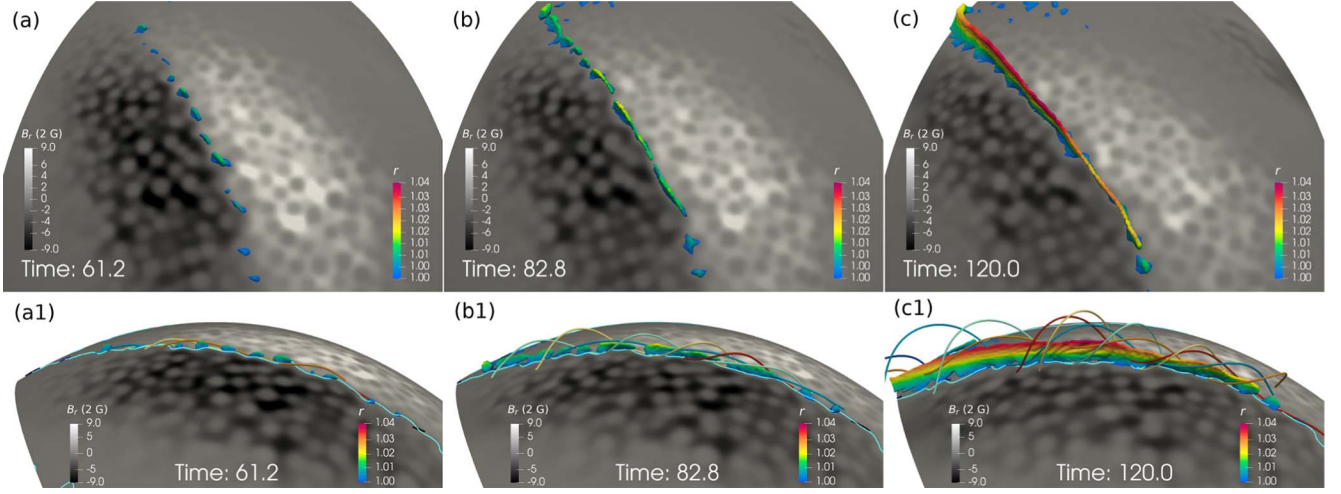


Figure 4. Formation of magnetic dip regions shown as isosurfaces colored by solar radius r from top views (a)–(c) and from side views (a1)–(c1) at times 61.2, 82.8, and 120. The surrounding magnetic field lines in different colors and the main PIL in cyan are plotted in (a1)–(c1) additionally. An animation of the side view of the formation of the magnetic dip regions is available in the online Journal. The animation proceeds from time 30 to 120 in steps of 0.6.

(An animation of this figure is available.)

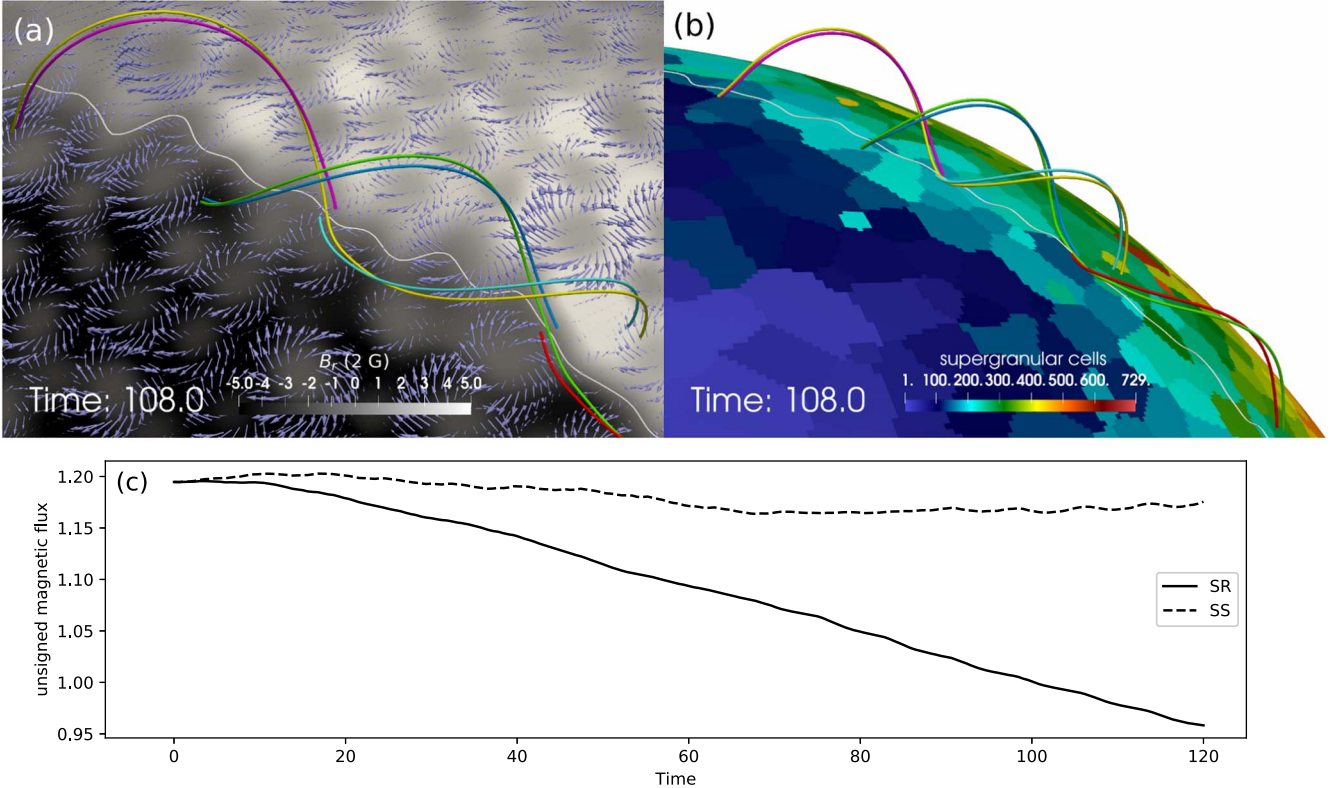


Figure 5. Linking sheared loops to helical field lines via photospheric magnetic reconnection along the white PIL. (a) Top view of six selected magnetic field lines above the photospheric magnetogram with arrows presenting horizontal velocity. (b) Side view of the same magnetic field lines in (a) above a photospheric color map presenting supergranular cells. (c) Evolution of the total unsigned magnetic flux on the photosphere for models SR (solid line) and SS (dashed line).

photosphere is plotted for both models. After a short period of flux dispersion without many cancellations, the unsigned magnetic flux of model SR decreases linearly, losing about 20% until time 120, which indicates continuous flux cancellation. The unsigned magnetic flux of model SS decreases less than 3% until time 70 and then slightly increases with small oscillations and slow flux cancellation. The slight increase is caused by the numerical error in the magnetic boundary condition.

4. Discussion and Conclusions

The only difference in model setup between models SR and SS is the vortical motions by Coriolis force, which leads to strikingly different results, namely, an MFR in model SR and potential arcades in model SS. The counterclockwise vortical flows in strong magnetic flux regions around supergranular boundaries inject negative magnetic helicity, which is accumulated along the PIL via helicity condensation to form a dextral filament channel in the northern hemisphere. Therefore,

Coriolis force is a key factor for helicity injection and formation of quiescent prominences, while effective magnetic flux diffusion by supergranular flows (Leighton 1964) and differential rotation are not the main reasons for the formation of filament channels. We will include the latitude dependence of the Coriolis effect (Duvall & Gizon 2000) in the future, expecting faster MFR formation at higher latitudes.

Helicity condensation theory describes how the injected magnetic helicity at small scales is transferred and condensed to the PIL, which explains the origin of strong axial magnetic flux along quiescent filament channels. But this theory can only lead to SMAs, which contradict the observational evidence (Bağ-Stęślicka et al. 2013; Wang & Stenborg 2010) of quiescent prominences. Previous numerical simulations on helicity condensation (Knizhnik et al. 2015, 2017; Zhao et al. 2015) did not produce MFRs because of the absence of the primary diverging motions of supergranules, which not only generate the magnetic network but also converge opposite magnetic polarities at the PIL and drive the magnetic reconnection between footpoints of SMAs, the magnetic flux cancellation in forming filament channels (Wang & Muglach 2007), and the formation of MFRs.

During the formation of the coherent MFR in model SR, a chain of small MFRs first forms along the PIL with fragmented small MDRs to host prominence plasma. Later on, these small MFRs and MDRs grow and merge with neighbors to form the mature MFR, which is consistent with the “head-to-tail” conceptual model of prominence formation proposed by Martens & Zwaan (2001). The isolated MDRs consisting of piled-up magnetic dips from the photosphere may correspond to the observed pillars or legs of quiescent prominences (Li & Zhang 2013; Zhou et al. 2021). We run models, starting with west-to-east PILs, to simulate high-latitude quiescent prominences and formed MFRs that will be reported in a follow-up paper.

This research was supported by the Basic Research Program of Yunnan Province (2019FB140, 202001AW070011), the National Natural Science Foundation of China (11803031, 12073022). We acknowledge discussions with Mark C. M. Cheung, George H. Fisher, and Shangbin Yang. The numerical simulations were conducted on the Yunnan University Astronomy Supercomputer.

Software: MPI-AMRVAC, PDFL_SS.

ORCID iDs

Chun Xia  <https://orcid.org/0000-0002-7153-4304>

References

- Amari, T., Luciani, J. F., Mikic, Z., & Linker, J. 1999, *ApJL*, **518**, L57
- Antiochos, S. K. 2013, *ApJ*, **772**, 72
- Bağ-Stęślicka, U., Gibson, S. E., Fan, Y., et al. 2013, *ApJ*, **770**, L28
- Berger, M. A., & Field, G. B. 1984, *JFM*, **147**, 133
- Bommier, V., Degl’Innocenti, E. L., Leroy, J. L., & Sahal-Brechot, S. 1994, *SoPh*, **154**, 231
- Cheung, M. C. M., & DeRosa, M. L. 2012, *ApJ*, **757**, 147
- DeVore, C. R., & Antiochos, S. K. 2000, *ApJ*, **539**, 954
- Duvall, T. L., & Gizon, L. 2000, *SoPh*, **192**, 177
- Egorov, P., Rädiger, G., & Ziegler, U. 2004, *A&A*, **425**, 725
- Fan, Y. 2001, *ApJL*, **554**, L111
- Fisher, G. H., Kazachenko, M. D., Welsch, B. T., et al. 2020, *ApJS*, **248**, 2
- Foukal, P. 1971, *SoPh*, **19**, 59
- Gardiner, T. A., & Stone, J. M. 2005, *JCoPh*, **205**, 509
- Gibson, S. E., Kucera, T. A., Rastawicki, D., et al. 2010, *ApJ*, **724**, 1133
- Gudiksen, B. V., & Nordlund, Å. 2005, *ApJ*, **618**, 1020
- Guo, Y., Xia, C., Keppens, R., & Valori, G. 2016, *ApJ*, **828**, 82
- Hathaway, D. H. 1982, *SoPh*, **77**, 341
- Hirzberger, J., Gizon, L., Solanki, S. K., & Duvall, T. L. 2008, *SoPh*, **251**, 417
- Knizhnik, K. J., Antiochos, S. K., & DeVore, C. R. 2015, *ApJ*, **809**, 137
- Knizhnik, K. J., Antiochos, S. K., DeVore, C. R., & Wyper, P. F. 2017, *ApJ*, **851**, L17
- Langfellner, J., Gizon, L., & Birch, A. C. 2015, *A&A*, **581**, A67
- Leighton, R. B. 1964, *ApJ*, **140**, 1547
- Leroy, J. L., Bommier, V., & Sahal-Brechot, S. 1983, *SoPh*, **83**, 135
- Li, L., & Zhang, J. 2013, *SoPh*, **282**, 147
- Mackay, D. H., DeVore, C. R., & Antiochos, S. K. 2014, *ApJ*, **784**, 164
- Mackay, D. H., Gaizauskas, V., & Yeates, A. R. 2008, *SoPh*, **248**, 51
- Mackay, D. H., Karpen, J. T., Ballester, J. L., Schmieder, B., & Aulanier, G. 2010, *SSRv*, **151**, 333
- Mackay, D. H., & van Ballegoijen, A. A. 2001, *ApJ*, **560**, 445
- Mackay, D. H., & Van Ballegoijen, A. A. 2006, *ApJ*, **641**, 577
- Martens, P. C., & Zwaan, C. 2001, *ApJ*, **558**, 872
- Olivares, H., Porth, O., Davelaar, J., et al. 2019, *A&A*, **629**, A61
- Ouyang, Y., Zhou, Y. H., Chen, P. F., & Fang, C. 2017, *ApJ*, **835**, 94
- Parenti, S. 2014, *LRSP*, **11**, 1
- Patsourakos, S., Vourlidas, A., Tãrãk, T., et al. 2020, *SSRv*, **216**, 131
- Pevtsov, A. A., & Neidig, D. 2005, in ASP Conf. Ser., 346 (San Francisco, CA: ASP), 219
- Pomoell, J., Lumme, E., & Kilpua, E. 2019, *SoPh*, **294**, 41
- Porth, O., Xia, C., Hendrix, T., Moschou, S. P., & Keppens, R. 2014, *ApJS*, **214**, 4
- Rondi, S., Roudier, T., Molodij, G., et al. 2007, *A&A*, **467**, 1289
- Schmieder, B., Roudier, T., Mein, N., et al. 2014, *A&A*, **564**, A104
- Schrijver, C. J., Hagenaar, H. J., & Title, A. M. 1997, *ApJ*, **475**, 328
- van Ballegoijen, A. A., Cartledge, N. P., & Priest, E. R. 1998, *ApJ*, **501**, 866
- Van Ballegoijen, A. A., & Martens, P. C. H. 1989, *ApJ*, **343**, 971
- Wang, Y.-M., & Muglach, K. 2007, *ApJ*, **666**, 1284
- Wang, Y.-M., & Stenborg, G. 2010, *ApJ*, **719**, L181
- Xia, C., & Keppens, R. 2016, *ApJ*, **823**, 22
- Xia, C., Keppens, R., Antolin, P., & Porth, O. 2014a, *ApJ*, **792**, L38
- Xia, C., Keppens, R., & Guo, Y. 2014b, *ApJ*, **780**, 130
- Xia, C., Teunissen, J., Mellah, I. E., Chanã, E., & Keppens, R. 2018, *ApJS*, **234**, 30
- Zhao, L., DeVore, C. R., Antiochos, S. K., & Zurbuchen, T. H. 2015, *ApJ*, **805**, 61
- Zhou, C., Xia, C., & Shen, Y. 2021, *A&A*, **647**, A112